PCCP

ROYAL SOCIETY OF CHEMISTRY

PAPER

Cite this: *Phys. Chem. Chem. Phys.*, 2023, **25**, 19116

The role of native point defects and donor impurities in the electrical properties of $ZnSb_2O_4$: a hybrid density-functional study†

Supparat Charoenphon,‡[a] Auttasit Tubtimtae,[b] Isao Watanabe,[c] Sirichok Jungthawan,[d] Jiraroj T-Thienprasert,[a] Adisak Boonchun[a] and Pakpoom Reunchan*[a]

The ceramic material zinc antimony oxide $ZnSb_2O_4$ has promising electrical and magnetic properties, making it suitable for various applications such as electrochemical and energy storage. However, the effects of point defects and impurities on its electrical properties have never been revealed. Here, we employ hybrid density-functional calculations to investigate the energetics and electronic properties of native point defects and donor impurities in $ZnSb_2O_4$. The energetically favorable configurations of native point defects under selected growth conditions (O-rich and O-poor) are identified based on the calculated formation energies. The study finds no shallow donor and shallow acceptor defects with low formation energies. Still, the oxygen vacancy (V_O) has the lowest formation energy among the donor-type defects under O-rich and O-poor conditions. However, it acts as a very deep acceptor, making it unlikely to provide free electron carriers to the conduction band. Moreover, electron carriers are likely to be compensated by the formation of zinc vacancies (V_{Zn}) and the zinc substituted for antimony (Zn_{Sb}), which behave as dominant acceptors. Our analysis of the charge neutrality conditions estimates that the Fermi level of undoped $ZnSb_2O_4$ would be pinned in a range that is 2.60 eV to 3.12 eV above the VBM for O-rich to O-poor growth conditions, respectively, suggesting that this material is semi-insulating. The possibility of enhancing free electron carriers by doping with Al, Ga, In, and F impurities is also investigated. Our results, however, indicate that high n-type conductivity is hindered by self-compensation in which the impurities additionally act as electron killers. Our results suggest that other impurity candidates and approaches may need to be considered to efficiently dope this material into n-type. Overall, this work paves the way for point defect engineering in this class of ternary oxides.

Received 31st March 2023,
Accepted 21st June 2023

DOI: 10.1039/d3cp01470c

rsc.li/pccp

1. Introduction

Metal chalcogenide semiconductors in the form of nanoparticles and thin films have previously been considered the most promising materials for electrocatalytic and electrochemical applications.[1–3] Electrochemical devices, however, are primarily focused on metals with earth abundance, non-toxicity, low cost, ionic charging and discharging capabilities, and safety during chemical reactions. One of the major interests is transition metal oxides with high potential performance in various technological applications. This includes optoelectronics, photovoltaics, photocatalysis, and energy storage devices such as supercapacitors and pseudocapacitors.[4] Most oxide materials have been used to investigate their electrochemical performances as electrodes. Several oxide materials have been investigated for their electrochemical properties. This has been done with consideration of various polymorphs and composites for these applications, for example, MoO_3,[5] Bi_2O_3,[6] WO_3,[7] and CuO.[8]

[a] *Department of Physics, Faculty of Science, Kasetsart University, Bangkok 10900, Thailand. E-mail: pakpoom.r@ku.ac.th*
[b] *Division of Physics, Department of Physical and Material Sciences, Faculty of Liberal Arts and Science, Kasetsart University, Kamphaeng Saen Campus, Nakhon Pathom 73140, Thailand*
[c] *Advanced Meson Science Laboratory, Nishina Center for Accelerator-Based Science, RIKEN, 2-1 Hirosawa, Wako 351-0198, Japan*
[d] *School of Physics, Institute of Science, Suranaree University of Technology, Nakhon Ratchasima, 30000, Thailand*

† Electronic supplementary information (ESI) available: Crystal structure and atomic coordinates of $ZnSb_2O_4$, Bader charge of $ZnSb_2O_4$, Sb_2O_3, and ZnO, comparison of formation energies and transition levels using 56 and 224-atom supercell, and local atomic structures of intrinsic defects and impurities. See DOI: https://doi.org/10.1039/d3cp01470c

‡ Current address: Advanced Meson Science Laboratory, Nishina Center for Accelerator-Based Science, RIKEN, 2-1 Hirosawa, Wako 351-0198, Japan.

One of the most fundamental materials that many researchers use worldwide is ZnO. It is well known that ZnO is a wide band-gap semiconductor with a wurtzite crystal structure that has been widely studied for industrial and technological applications. Due to its high n-type conductivity and band gap of 3.2–3.4 eV, ZnO is an exciting and promising material for transparent electrodes in optoelectronics. While it is feasible to dope ZnO with high electron carriers with donor impurities such as aluminum,[9,10] doping ZnO into p-type remains challenging. The application of ZnO as an electronic material is, therefore, still limited. Alternatively, ZnO has been studied in electrochemical and energy storage applications. Many efforts have been made to introduce other cations such as Co, Al, Fe, Ga, and Cr into ZnO to obtain various Zn-based ternary metal oxides (TMOs), including $ZnCo_2O_4$,[11] $ZnAl_2O_4$,[12] $ZnFe_2O_4$,[13] $ZnGa_2O_4$,[14] and $ZnCr_2O_4$.[15] These TMOs are expected to have improved structural stability and electrochemical performances for energy storage and capacitive devices.

Incorporating a Sb cation into ZnO results in the formation of $ZnSb_2O_4$, a spinel ternary metal oxide with an identical structure to other Sb-based oxides in the MSb_2O_4 family where M is either a small divalent or transition metal.[16] While less studied than other metal oxides, $ZnSb_2O_4$ can potentially be used in sensors, non-linear devices, and pseudo- and super-capacitors. $ZnSb_2O_4$ has a tetragonal structure with a space group of $P42/mbc$ (135) at room temperature, similar to the mineral spinel class tetragonal Pb_3O_4. The crystal structure of $ZnSb_2O_4$ shown in Fig. 2 consists of a rutile-related chain of ZnO_6 octahedral along the c-axis linked by a trigonal pyramidal Sb^{3+} cation bound to three oxygen ions. It possesses a lone pair of electrons which can be regarded as a fourth ligand. The Zn atoms have an octahedral position in the crystal structure, and the Sb atoms make a triangular pyramidal structure with oxygen atoms.[17] It was reported that the crystalline phase $ZnSb_2O_4$ synthesized using the solid-state synthesis technique yields an optical band gap of 4.7 eV and lattice parameters $a = b = 8.5153$ Å and $c = 5.9349$ Å. The investigation into improving the electrical properties and specific characteristics of $ZnSb_2O_4$ revealed that the material could be used as a non-linear device.[18–20] Recently, Raknual *et al.* demonstrated the simple synthesis and investigated the potential of undoped and In^{3+} doped-$ZnSb_2O_4$ for their pseudocapacitive charge storage properties.[21] The study found that In^{3+} doping could enhance the energy density, power density, and specific capacitance in $ZnSb_2O_4$. Nevertheless, the In^{3+}-doped $ZnSb_2O_4$ may lead to electrode degradation. Then, self-discharge and diffusion processes can occur due to the fast kinematics in the electrode interfaces. Thus, the effects of doping with impurities on the electronic properties of $ZnSb_2O_4$ are a topic of significant interest and merit further investigation.

Point defects are known to significantly impact the electronic properties of materials, including metal oxide semiconductors. It is widely accepted that lattice defects, particularly intrinsic ones, are unavoidable in the growth processes at finite temperatures. Intrinsic defects significantly control the electrical and optical properties of semiconductors. Introducing a small number of foreign atoms into materials can drastically alter their electrical conductivity. A better understanding of how these defects affect the electronic properties of $ZnSb_2O_4$ could result in improved capacitive properties.

Density-functional theory (DFT) has been widely recognized as a powerful tool for studying the behavior of defects and impurities in various materials. DFT studies have revealed the role of point defects and dopants in various crystal structures of ternary metal oxides, such as perovskites and spinels. While many authors devoted extensive studies on the point defects and impurities in perovskite oxides such as $SrTiO_3$,[22–24] $BaTiO_3$,[25–27] and $BaSnO_3$,[28–30] and spinel oxides such as a series of A_2BO_4 where A and B are either III-valent and II-valent cation ions,[31] $ZnMn_2O_4$ where M = Co, Rh, Ir,[32,33] much less has been done in Pb_3O_4-type antimony oxides. The source of either n-type or p-type conductivity, the effects of point defects on thermoelectric properties, and the proposal to overcome the doping limit in those ternary metal oxides have been revealed.

Despite $ZnSb_2O_4$ being discovered as an industrial functional material many years ago, little is known about how defects affect electrical properties. It is, therefore, necessary to understand native defects and dopant impurities and control their formation in $ZnSb_2O_4$. As far as we know, only the generalized gradient approximation (GGA) calculations are published in conjunction with the experiments on doped $ZnSb_2O_4$.[21] The GGA-functional calculations would, however, be limited by the band gap problem and the self-interaction error, which can reduce their accuracy and lead to inaccurate defect levels and formation energies.

Our aim in the present work is to investigate the likelihood of the formation of native point defects and the electronic properties of these defects using the screened hybrid-functional proposed by Heyd, Scuseria, and Ernzerhof (HSE).[34] First, we determine the bulk properties of $ZnSb_2O_4$, such as lattice parameters, electronic structure, bang-edge position, formation enthalpy, and equilibrium growth chemical potential diagram. We then explore the thermodynamic stability of all possible native defects in $ZnSb_2O_4$, including zinc, antimony, and oxygen vacancies (V_{Zn}, V_{Sb}, and V_O), the interstitials (Zn_i, Sb_i, and O_i) and the antisites (Sb_{Zn}, Zn_{Sb}, Sb_O, Zn_O, O_{Sb} and O_{Zn}) through the formation energies calculated under representative growth conditions. The local atomic structure and electrical properties of these defects are examined. The results show that carrier compensation due to the native defects is likely to make as-grown $ZnSb_2O_4$ semi-insulating. In addition, we investigate the energetics and electronic properties of cation and anion impurities such as Al, Ga, In, and F, which are expected to act as donors. We will discuss how these impurities affect the Fermi level and, therefore, the possibility of n-type doping in $ZnSb_2O_4$.

2. Computational methods

Our DFT calculations were performed using the HSE screened-hybrid-functional (HSE) implemented in the VASP code.[35] The Hartree–Fock (HF) mixing parameter $\alpha = 0.48$ and a standard

Table 1 Calculated structural parameters, formation enthalpy (ΔH_f), and band gap (E_g) of $ZnSb_2O_4$. The available experimental values are also listed

	PBE	HSE (α = 0.25)	HSE (α = 0.48)	Experimental
a (Å)	8.656	8.584	8.526	8.515
c (Å)	6.081	5.959	5.838	5.934
ΔH_f (eV)	−9.56	−9.88	−10.25	−11.05[a]
E_g (eV)	2.74	3.77	4.73	4.70

[a] Estimated using the ΔH_f of ZnO and Sb_2O_3 through Hess's Law as $\Delta H_f(ZnSb_2O_4) = \Delta H_f(ZnO) + \Delta H_f(Sb_2O_3)$.

screening length of 10 Å were used, giving a band gap and equilibrium lattice parameters in good agreement with the experimental values in Table 1. An energy cut-off of 520 eV was used for the plane-wave basis set expansion. The valence electron configurations of the projector augmented wave pseudopotentials are $3d^{10}4s^2$ for Zn, $4d^{10}5s^25p^3$ for Sb, and $2s^22p4$ for O. For calculations of the lattice parameters, band gaps, and formation enthalpies, a 28-atom primitive cell was employed with 3 × 3 × 3 Monkhorst–Pack meshes for the integrations over the Brillouin zone. For calculations of the native defects, including the vacancies (V_{Zn}, V_{Rh} and V_O), the cation antisites (Zn_{Sb}, Sb_{Zn}) and the interstitials (Zn_i, Sb_i, and O_i), we adopted a 56-atom supercell which is a 1 × 1 × 2 repetition of the primitive cell. This supercell was also adopted to calculate the donor impurities, including the substitutions (Al_{Zn}, Ga_{Zn}, and In_{Zn}) and the interstitials (Al_i, Ga_i, and In_i). For the integration over the Brillouin zone, we used non-Γ-centered 2 × 2 × 2 Monkhorst–Pack meshes. Test calculations using a 224-atom supercell which is a 2 × 2 × 2 repetition of the primitive cell with the (1/4,1/4,1/4) special k point, show that the formation energy differences of the point defects are converged within 0.15 eV. At the same time, the corresponding thermodynamic transition levels converged within 0.10 eV (see the ESI†). Note that spin–orbit coupling has minor effects on the formation energies and transition levels.

The formation energy of a defect D in charge state q was calculated as

$$E_f(D^q) = E_{tot}(D^q) - E_{tot}(ZnSb_2O_4) - \sum n_i\mu_i + q(\varepsilon_F + E_v) + E_{corr}(D^q), \quad (1)$$

where $E_{tot}(D^q)$ is the total energy of the cell with defect D in the charge state q. $E_{tot}(ZnSb_2O_4)$ is the total energy of the supercell without defects, n_i is the number of atoms of species i (Zn, Sb or O) that have been added to ($n_i > 0$) or removed from ($n_i < 0$) the supercell. For a charged defect, the electron(s) is removed or added to the Fermi level (ε_F), referenced to the valence band maximum (VBM, E_v). These atoms are taken from or placed into the reservoir with energy μ_i, where the chemical potentials $\tilde{\mu}_i$ are referenced to the energy per atom of isolated elemental phase as $\tilde{\mu}_{Zn} = \mu_{Zn} - E_{tot}[Zn_{bulk}]$, $\tilde{\mu}_{Sb} = \mu_{sb} - E_{tot}[Sb_{bulk}]$ and $\tilde{\mu}_O = \mu_O - E_{tot}[O_2]$. The energy per atom of these elemental phases was obtained by our DFT calculations; the total energy per atom of bulk Zn and Sb and half of the total energy of an isolated O_2 molecule were calculated as −1.53 eV, −6.46 eV, and −8.95 eV, respectively. The correction energy, $E_{corr}(D^q)$, due to the spurious electrostatic interactions between periodic charged finite-size supercell proposed by Freysoldt *et al.* was also added to the formation energy of the charged defect.[36] The static dielectric constant (ε_0) of $ZnSb_2O_4$ used in the correction is 13.04, as estimated by the density-functional perturbation theory implemented in the VASP code.[37]

The chemical potential $\tilde{\mu}_i$ can, in principle, vary, representing the growth conditions such as oxygen pressure and temperature. However, it must satisfy the thermodynamic equilibrium condition of $ZnSb_2O_4$, $\tilde{\mu}_{Zn} + 2\tilde{\mu}_{Sb} + 4\tilde{\mu}_O = \Delta H_f(ZnSb_2O_4)$ where $\Delta H_f(ZnSb_2O_4)$ is the formation enthalpy of $ZnSb_2O_4$. Our calculated $\Delta H_f(ZnSb_2O_4)$ by the HSE functional with α = 0.48 is −10.43 eV, slightly lower than the values obtained by the standard HSE06 and the PBE functionals (Table 1). This value is comparable to the experimental $\Delta H_f(ZnSb_2O_4)$ estimated following Hess's law of −11.05 eV.[38] The following constraints are implemented to avoid precipitation of the unwanted compounds ZnO, Sb_2O_3, and Sb_2O_5: $\tilde{\mu}_{Zn} + \tilde{\mu}_O < \tilde{\mu}_{ZnO}$, $2\tilde{\mu}_{Sb} + 3\tilde{\mu}_O < \tilde{\mu}_{Sb_2O_3}$ and $2\tilde{\mu}_{Sb} + 5\tilde{\mu}_O < \tilde{\mu}_{Sb_2O_5}$. The metallic Zn and Sb, and gaseous O_2 are also taken as the upper bounds for $\tilde{\mu}_{Zn}$, $\tilde{\mu}_{Sb}$, and $\tilde{\mu}_O$. These constraints defined a domain in a three-dimensional chemical potential diagram as shown in Fig. 1. For a stable thermodynamic equilibrium growth of $ZnSb_2O_4$, $\tilde{\mu}_{Zn}$, $\tilde{\mu}_{Sb}$ and $\tilde{\mu}_O$ must lie within this domain (pink shaded area). In the present work, we show the formation energies calculated using the chemical potentials corresponding to the O-rich (point A), $\tilde{\mu}_O$ = 0 and O-poor (point B) growth conditions $\tilde{\mu}_O = [\Delta H_f(ZnSb_2O_4) - \tilde{\mu}_{Zn} - 2\tilde{\mu}_{Sb}]/4$ = −0.79 eV. The formation energies for other growth conditions can be selectively calculated using $\tilde{\mu}_{Zn}$, $\tilde{\mu}_{Sb}$, and $\tilde{\mu}_o$ in the pink-shaded area. The chemical

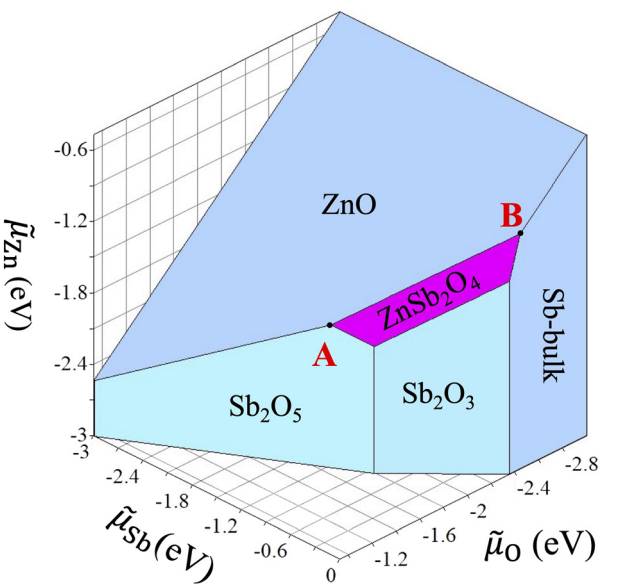

Fig. 1 The thermal equilibrium growth conditions allowed for $ZnSb_2O_4$ (pink shaded area). The chemical potentials of the Sb ($\tilde{\mu}_{Sb}$), Zn ($\tilde{\mu}_{Zn}$), and O ($\tilde{\mu}_O$), are referenced using the energy per atom of Sb and Zn metals and the O_2 molecule. Labels A and B denote the O-rich and O-poor limits representing the extreme growth conditions, respectively.

Table 2 Formation enthalpies of ZnO, Sb_2O_3, Sb_2O_5, Al_2O_3, Ga_2O_3, In_2O_3, and ZnF_2 obtained using the PBE functional and the HSE functional (α = 0.48). The experimental values are also listed

	ΔH_f (eV)		
Material	PBE	HSE	Experimental
ZnO	−2.81	−3.35	−3.63
Sb_2O_3	−6.81	−6.82	−7.42
Sb_2O_5	−8.87	−10.28	−10.44
Al_2O_3	−8.07	−8.85	−9.60
Ga_2O_3	−15.18	−16.87	−17.37
In_2O_3	−9.44	−10.78	−11.29
ZnF_2	−6.84	−8.09	−7.92

potentials of Al, Ga, In and F are limited by the formation of Al_2O_3, Ga_2O_3, In_2O_3, and ZnF_2, under both O-rich and O-poor conditions, respectively; $\tilde{\mu}_{Al} = (\Delta H_f(Al_2O_3) - 3\tilde{\mu}_O)/2$, $\tilde{\mu}_{Ga} = (\Delta H_f(Ga_2O_3) - 3\tilde{\mu}_O)/2$, $\tilde{\mu}_{In} = (\Delta H_f(In_2O_3) - 3\tilde{\mu}_O)/2$, and $\tilde{\mu}_{Zn} = (\Delta H_f(ZnF_2) - 3\tilde{\mu}_F)$, where $\Delta H_f(Al_2O_3)$, $\Delta H_f(Ga_2O_3)$, $\Delta H_f(In_2O_3)$, and $\Delta H_f(Zn_2F)$ are the formation enthalpy of Al_2O_3, Ga_2O_3, In_2O_3, and ZnF_2 obtained by the HSE functional with α = 0.48. These are listed in Table 2, along with the corresponding experimental values.[39]

The positions of the conduction band (CB) and valence band (VB) edges of $ZnSb_2O_4$ were determined using the following empirical equations:

$$E_{CB} = \chi(ZnSb_2O_4) - E_e - 0.5E_g, \quad (2)$$

and $E_{VB} = E_{CB} + E_g$, where E_{VB} and E_{CB} are the valence band and conduction band edge potentials, respectively. χ is the Mulliken electronegativity of $ZnSb_2O_4$, which is calculated as $\chi(ZnSb_2O_4) = \{[\chi(Zn)][\chi(Sb)]^2[\chi(O)]^4\}^{(1/5)} = 6.16$ eV where χ(Zn), χ(Sb), and χ(O) are the electronegativity of the neutral Zn, Sb, and O atoms, respectively.[40] E_e is the energy of free electrons on the hydrogen scale (~4.5 eV), and E_g is the calculated band gap using the HSE functional.

3. Results and discussion

3.1 Structural properties

Fig. 2 shows the primitive cell and local atomic structure of $ZnSb_2O_4$, a spinel mineral structurally identical to Pb_3O_4. Only a few ternary oxides, including, $CoSb_2O_4$,[16] $NiSb_2O_4$,[16] and $SnTi_2O_4$,[41] have this unique crystal structure. As listed in Table 1, the lattice parameters given by the HSE functional (with both 25% and 48% HF mixing parameters) agree very well with the experimental values within 2%. There are 28 atoms in the tetragonal primitive cell of $ZnSb_2O_4$ shown in Fig. 2(a), consisting of 4 Zn, 8 Sb, and 16 O. All figures of ball and stick models including the 3D isosurface of the charge density, were made using the VESTA software package.[42] It was suggested that the hollow in the center of the cell is stabilized by van der Waals interaction between lone pair electrons.[41,43] The local atomic structures of the Zn, the Sb, and the two inequivalent O atoms are shown in Fig. 2(b) and (e). Through distorted octahedral coordination, the Zn atom forms bonds with six neighboring O atoms with the two sets of O–Zn–O bond angles

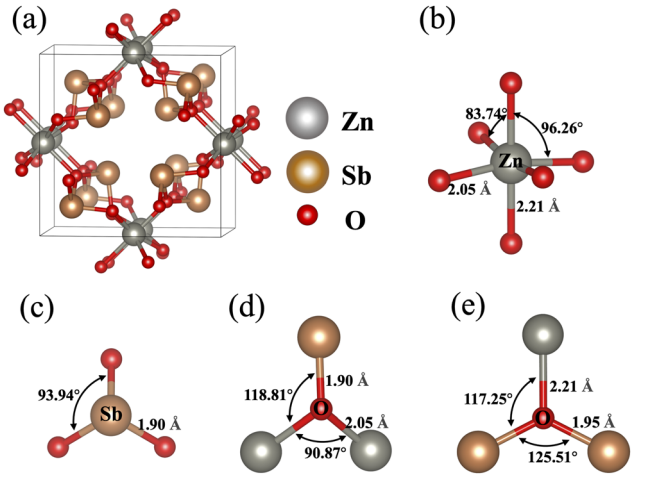

Fig. 2 (a) An illustration of $ZnSb_2O_4$ primitive cell containing 28 atoms and the its local atomic structure. (b) Zn, (C) Sb, (c) type-I O, and type-II O atoms. The calculated equilibrium Zn–O and Sb–O bond lengths and angles are also listed.

of ~83.74° and ~96.26° and the two sets of Zn–O bond lengths of 2.05 and 2.21 Å. The Sb atom is trigonal pyramidally coordinated with three O atoms (with an Sb–O bond length of 1.90 Å and an O–Sb–O bond angle of ~93.94°). The type-I O atom forms asymmetric trigonal pyramidal bonds with two Zn and one Sb neighboring atoms, as shown in Fig. 2(d). These two Zn–O bonds are equivalent with bond lengths of 2.05 Å, while the Sb–O bond length = 1.90 Å. On the other hand, the type-II O atom forms asymmetric trigonal planar bonds with two Sb atoms (Sb–O bond lengths = 1.95 Å) and one neighboring Zn atom (Zn–O bond length = 2.21 Å), as shown in Fig. 2(e). These bond lengths agree with the values obtained *via* empirical methods based on neutron diffraction experiments.[17] As can be observed from the Bader charge analysis (Table S1, ESI†),[44,45] Sb atoms in $ZnSb_2O_4$ (+1.86*e*) and Sb_2O_3 (+1.92*e*) are almost equally positively charged, indicating the presence of Sb^{3+} ions in $ZnSb_2O_4$. Since the atoms of type-I and type-II O in $ZnSb_2O_4$ are more negative (−0.20*e* to −0.26*e*) than the O atoms in ZnO along with the atoms of Zn in $ZnSb_2O_4$ being more positive, $ZnSb_2O_4$ will likely be more ionic than ZnO. This results in $ZnSb_2O_4$ having stronger electrostatic interactions between the cations and anions, making it more ionic than ZnO. Additionally, the larger size of Sb^{3+} compared to O^{2-} leads to higher coordination numbers, further increasing the ionic character of $ZnSb_2O_4$, evident by its larger band gap (~4.7 eV)19 compared to ZnO (~3.3 eV).[46]

3.2 Electronic structure

Fig. 3 shows the calculated projected density of states (PDOS), electronic band structure, and the electronic charge distribution associated with the band edges of $ZnSb_2O_4$. The PDOS in Fig. 3(a) indicates that the valence band is mainly dominated by O 2p states, with notable localized Zn 3d lying at ~−8 eV below the top of the valence band. There is also a small contribution from Sb 5s states to most regions of the valence band. The contribution of Sb 5p in the valence band is relatively minor;

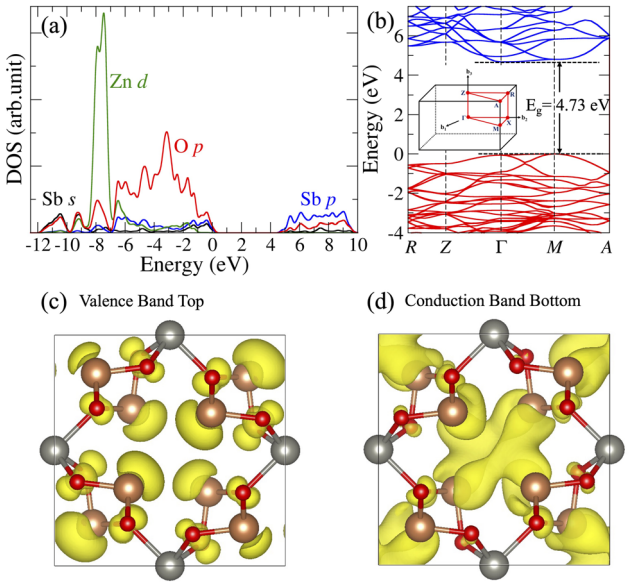

Fig. 3 (a) The calculated projected density of states (PDOS), (b) electronic band structure, and the electronic charge distribution associated with (c) the valence band, and (d) the conduction band edges of $ZnSb_2O_4$. The valence band maximum is set to 0 eV. The Brillouin zone of the $ZnSb_2O_4$ crystal structure is also shown as an inset in (b). The isosurface of the charge distribution is set to 8% of the maximum.

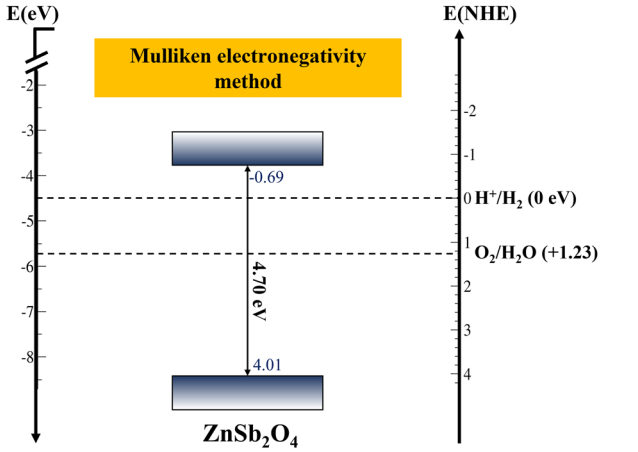

Fig. 4 Calculated valence and conduction band edge position of $ZnSb_2O_4$ obtained from the Mulliken electronegativity in the absolute energy scale (left vertical axis) and the natural hydrogen electrode scale (right vertical axis). The horizontally aligned numbers are the band edge positions on the NHE scale.

however, it results in the lone pair electrons at the top of the valence band, of which the charge density is shown in Fig. 3(c). A similar observation has been made in Sn_2TiO_4, where Sn 5p is mixed in the valence band, and lone pair electrons are formed.[41] The Sb 5p also constitutes most of the conduction band bottom, displaying antibonding properties (Fig. 3(d)). The calculated band structure of $ZnSb_2O_4$ is shown in Fig. 3(b). The electronic band gap is indirect since the valence band maximum (VBM) occurs at the M point, and the conduction band minimum (CBM) occurs at the Γ point. However, the difference between the valence band maxima at the M and Γ is only 0.06 eV, indicating that a strong onset of optical absorption can be expected. As shown in ref. 19 this is consistent with the experimental optical absorption. Table 1 illustrates that while the PBE functional accurately predicts lattice parameters and formation enthalpy, it significantly underestimates the electronic band gap. The calculated band gap using the PBE functional is nearly half the experimental value. Utilizing the standard HSE functional, with a mixing parameter of α = 0.25, results in a more accurate band gap prediction. However, a mixing parameter of α = 0.48 is necessary to achieve the experimental value of 4.7 eV.

Single crystal or thin film $ZnSb_2O_4$ exhibits a wide band gap, which renders it transparent or translucent, depending on the presence and distribution of native defects and impurities. Furthermore, its ultra-wide band gap makes it a promising candidate for ultraviolet photocatalysis and optoelectronics.[47] To fully realize the potential of this material in these fields, it is essential to determine the absolute band edge positions. In addition, the efficiency of n-type or p-type doping in semiconductors largely depends on the band edge positions of the host materials. Here, we adopted the standard approach based on the geometric mean of the Mulliken electronegativity (χ) for the constituent atoms of $ZnSb_2O_4$ to estimate the position of the band edges. This approach has been successfully applied in various oxides and other semiconductor materials.[48,49] The band edge positions of $ZnSb_2O_4$ calculated using the Mulliken electronegativity approach are presented in Fig. 4. The valence band edge potentials (*vs.* NHE) were +4.01 eV for $ZnSb_2O_4$ and +2.91 eV for TiO_2. These values indicate that both materials possess sufficiently positive valence band edge potentials with respect to the oxidation potential of water (+1.23 eV *vs.* NHE), making them active for photocatalytic O_2 production. The relatively low conduction band edge suggests that this material could be feasibly doped into n-type. The band edge positions for TiO_2 determined by our calculations were in excellent agreement with those reported by Schoonen *et al.*[49] However, to the best of our knowledge, band edge positions of $ZnSb_2O_4$ have not been reported in the literature. While providing a plausible description of the absolute band edge positions, our approach may yield results that diverge considerably from those obtained through other methodologies, such as band alignment with slab models.[50]

3.3 Energetics and electrical properties of intrinsic defects

To better understand the impact of intrinsic defects on the properties of $ZnSb_2O_4$, we extensively examine all possible intrinsic point defects in this material. Intrinsic defects have been known to significantly affect a wide range of properties in oxides, including optical and electrical properties. Our analysis focuses on the effects of various intrinsic point defects, including vacancies of Zn, Sb, and O atoms (V_{Zn}, V_{Sb}, and V_O), as well as interstitials (Zn_i, Sb_i, and O_i) and antisites (Sb_{Zn}, Zn_{Sb}, Sb_O, Zn_O, O_{Sb}, and O_{Zn}). Fig. 5 shows the formation energies obtained from our hybrid DFT calculations as a function of the Fermi level for the O-rich and O-poor conditions,

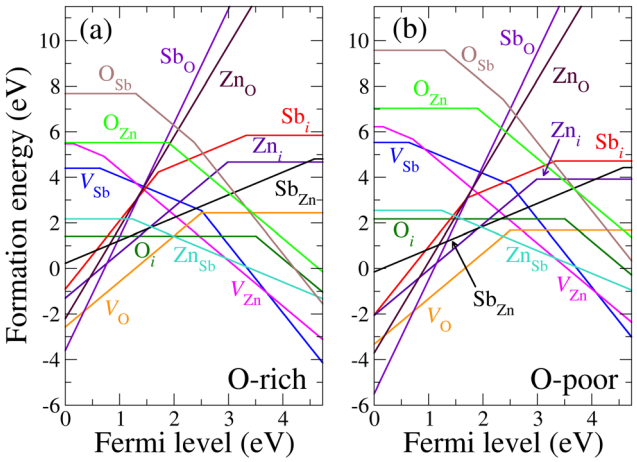

Fig. 5 Formation energies as a function of Fermi level position for native point defects in $ZnSb_2O_4$. The results are shown for (a) the O-rich limit and (b) the O-poor limit. The zero of the Fermi level corresponds to the VBM and CBM. Only segments corresponding to the lowest energy charge states are shown. The slope of each segment indicates the charge state. Kinks in the lines for the same defect indicate the thermodynamic transition levels.

corresponding to points A and B in Fig. 1, respectively. Their local atomic structures are shown in Fig. S1–S3 (ESI†). Here, we focus only on the isolated intrinsic defects, excluding the defect complexes between them. VBM and CBM are the lower and upper limits of the Fermi level, respectively. In Fig. 5, the formation energy plots show only the charge states of the defect with the minimum formation energy at a given Fermi level. The slope of the line reflects the most stable charge state of a defect. The kinks in the formation energy plots indicate the thermodynamic transition levels of the defect $\varepsilon(q/q')$, which has been extensively discussed in the literature.[33,51,52] The values of $\varepsilon(q/q')$ reported here are with respect to the VBM.

A. Intrinsic donor defects. As shown in Fig. 5, the donor defects are V_O, Sb_{Zn}, Sb_i, Zn_i, Sn_O, and Zn_O. Under both O-rich and O-poor conditions, V_O has the lowest formation energy among other donor defects. It is stable in 2+, and neutral charge states, while the 1+ charge state is unstable, indicating that it is a double donor with a negative-U behavior. This behavior of V_O has been reported in many oxides, including ZnO[53] and $BaSnO_3$.[29] We find that V_O is a deep donor with the transition level $\varepsilon(2+/0)$ = 2.50 eV. The high formation energy (almost 2 eV even under the O-poor conditions) when ε_F is close to the CBM (n-type conditions) suggests that the concentration of V_O will be low. However, the low formation energy of V_O when ε_F approaches the VBM (p-type conditions) where V_O assumes the 2+ charge state suggests that oxygen vacancies can be compensating centers for p-type doping in this material. In a neutral compound, the collective sum of the oxidation states of all its atoms or ions is zero. The oxidation states of Zn, Sb, and O atoms in $ZnSb_2O_4$ are thus reasonably assumed to be 2+ and 3+, and 2−, respectively. The antisite Sb_{Zn}, in which Sb is substituted for Zn, can, thus, act as a single donor. Fig. 5 shows that Sb_{Zn} is stable in the 1+ and neutral charge states with $\varepsilon(1+/0)$ = 4.58 eV above the VBM, very close to the CBM, which indicates it is nearly a shallow donor. Cation interstitials, *i.e.*, Zn_i and Sb_i, also act as donors. These defects can donate multiple electrons to their neighboring O atoms, thus are positively charged. Our findings indicate that Zn_i is stable in the 2+ and neutral charge states, while Sb_i is stable in the 3+, 1+, and neutral charge states. Additionally, we have determined the thermodynamic transition levels for Zn_i ($\varepsilon(2+/0)$ = 2.99 eV) and Sb_i ($\varepsilon(3+/1+)$ = 1.71 eV and $\varepsilon(1+/0)$ = 3.33 eV). These levels indicate that both Zn_i and Sb_i are deep donors. Their high formation energies under n-type conditions for both O-rich and O-poor conditions suggest low concentrations. Thus, they are unlikely to contribute to n-type conductivity in $ZnSb_2O_4$. The formation of antisite defects, where the cations (Sb and Zn) are substituted for oxygen atoms Sb_O and Zn_O, is energetically unfavorable under n-type conditions. This can be attributed to the large disparity in ionic radii between the cations (Sb: 0.76 Å, Zn: 0.74 Å) and oxygen (1.40 Å),[54] leading to the significant off-site displacement of the cations and thus, resulting in high formation energies. Nevertheless, these antisite defects may be able to compensate for hole carriers in p-type $ZnSb_2O_4$ due to their low formation energies.

B. Intrinsic acceptor defects. For Zn vacancy, the missing Zn atom breaks six Zn–O bonds, creating six dangling O bonds and two holes. We find that V_{Zn} is a double acceptor, which can occur in the neutral, 1−, and 2− charge states. This finding is like those in $ZnRh_2O_4$ and ZnO in which V_{Zn} acts as a double acceptor.[33,55] The hole states are found to be located well above the VBM, making V_{Zn} a deep acceptor with $\varepsilon(0/1-)$ = 0.16 eV, and $\varepsilon(1-/2-)$ = 0.71 eV, as shown in Fig. 5. Removal of the Sb atom would break three Sb–O bonds, resulting in three holes. These hole states lie in the band gap and can accept up to three additional electrons. This, thus, makes V_{Sb} a triple acceptor with $\varepsilon(0/1-)$ = 0.67 eV, and $\varepsilon(1-/3-)$ = 2.50 eV. Although the removal of the Zn atom involves breaking six Zn–O bonds, the removal of the Sb atom involves breaking only three Sb–O bonds, and their formation energies are comparable. The comparable formation energy is likely due to the Sb–O bonds being more potent than the Zn–O bonds, as evidenced by the shorter average Sb–O bond length (1.90 Å) than the average Zn–O (∼2.13 Å). As a result, breaking three strong Sb–O bonds cause comparable energy compared to breaking six Zn–O bonds. These cation vacancies act as acceptors and have a high formation energy (low concentration) under O-rich and O-poor conditions for Fermi levels near the VBM (p-type conditions). However, their low formation energies when the Fermi levels approach the CBM indicate that V_{Zn} and V_{Sb} can be compensating centers for n-type doping. Owing to the oxidation state of Zn (2+), and Sb (3+), Zn substituted for Sb, Zn_{Sb} is expected to act as a single acceptor. Zn_{Sb} is stable in the neutral and 1− charge states with $\varepsilon(0/1-)$ = 1.24 eV, indicating that it is a deep acceptor. Since the ionic radius of Zn^{2+} is slightly smaller than that of Sb^{3+}, the substitution of Zn for the Sb atom is expected to be feasible. This is indicated by the relatively low formation energy of Zn_{Sb} under both growth conditions (Fig. 5).

Other acceptors include oxygen interstitial (O_i), O substituted for Zn (O_{Zn}), and O substituted for Sb (O_{Sb}). Due to its

surrounding cations, O_i can draw two electrons and become a double acceptor. Fig. 5 shows that O_i is a very deep acceptor, which is stable in the neutral and 2− charge states. For most ε_F positions, O_i is electrically inactive, but for the positions above $\varepsilon(0/2-) = 3.50$ eV, it is doubly negatively charged. The relatively high formation energy of O_i makes it unlikely to take part in the charge carriers of the material. O_{Zn} is characterized by significant offsite displacements toward the nearby O atom, forming an O–O bond with a bond length ranging from 1.28–1.41 Å, as depicted in Fig. S3(d) (ESI†). It can accept up to two electrons as a double acceptor, with $\varepsilon(0/2-) = 1.90$ eV. Large offsite displacements toward the nearby O atom and the formation of an O–O bond (with the bond length ranging from 1.19–1.42 Å) are also observed for O_{Sb} (Fig. S3(c), ESI†). It acts as a deep acceptor, characterized by the $\varepsilon(0/2-) = 1.30$ eV and $\varepsilon(2-/3-) = 2.37$ eV. The formation energies of O_{Zn} and O_{Sb} are very high for ε_F near the VBM under both O-rich and O-poor conditions. Hence, we expect their concentrations to be negligible under equilibrium growth conditions. However, O_{Zn} and O_{Sb} can behave as compensating centers for donor impurities because of their reasonably low formation energies for ε_F near the CBM.

Based on the above discussion, we have revealed the electrical behavior of all intrinsic point defects in $ZnSb_2O_4$. The dominant donor and acceptor defects have also been identified. Whether this material is naturally n-type, p-type, or semi-insulating. To answer this question, we estimate the pinned ε_F by considering the charge neutrality conditions in a semiconductor with defects, which requires that

$$\sum_i q_i c(D_i^{q_i}) + p_0 - n_0 = 0, \quad (3)$$

where $c(D_i^{q_i})$ is the concentration of a defect D_i in charge state q_i, which can be calculated, at given ε_F, using the formation energy of the defect described in eqn (1). n_0 is the electron concentration in the conduction band, and p_0 is the hole concentration in the valence band as estimated by the Boltzmann approximation. A description of the detailed expressions for $c(D_i^{q_i})$, n_0, and p_0 can be found in our previous work and other works.[33,56] For the calculations of n_0, and p_0, the electron (m_e) and hole (m_h) effective masses are required. The calculated band structure of $ZnSb_2O_4$, as presented in Fig. 3(b), exhibits a significant anisotropy in the conduction band edge. The curvature of the band edge varies greatly between the Γ–M and Γ–Z directions, resulting in disparate electron effective masses for each reciprocal vector direction. Our calculated $m_e(\Gamma\text{–}M) = 5.65m_0$ and $m_e(\Gamma\text{–}Z) = 0.86m_0$, where m_0 is the electron rest mass. The average m_e is estimated as $\left[m_e(\Gamma - Z)^2 m_e(\Gamma - M)\right]^{\frac{1}{3}} = 0.86m_0$, following the assumption of the density of states effective mass.[57] We also find a substantial anisotropy in the valence band edge where the VBM is at M. Using an analogous procedure, the average m_h is estimated as $\left[m_e(M - \Gamma)^2 m_e(M - A)\right]^{\frac{1}{3}}(4)^{\frac{2}{3}} = 18.43m_0$ (M point is 4-fold degeneracy in the Brillouin zone). The average m_e and m_h are then used to calculate n_0 and p_0, respectively. Based on Fig. 5, it can be assumed that the electrically active low-energy defects that contribute significantly to charge neutrality in eqn (3) are V_{Zn}, V_{Sb}, and Zn_{Sb}. At a typical growth temperature of 400 K, the charge neutrality gives rise to the Fermi level pinning at values ranging from 2.39 eV to 2.80 eV above the VBM for the O-rich to O-poor growth conditions, respectively. This observation indicates that as grown, $ZnSb_2O_4$ is a semi-insulating material with very weak n-type behavior as the pinned Fermi levels lie slightly above half of the band gap (4.7 eV). In the next section, we explore the possibility of doping $ZnSb_2O_4$ into n-type material by external impurities.

3.4 Energetics and electrical properties of donor impurities

To utilize $ZnSb_2O_4$ in practical applications such as pseudocapacitive devices, enhancing charge carriers is often required. This material may be feasible for n-type doping based on the relatively low position of the conduction band edge, as shown in Fig. 4. Here, we investigate the possibility of doping with impurities expected to act as electron donors, including Al, Ga, In, and F. The likelihood of these impurities was investigated through the calculated formation energies as a function of the Fermi level. For the metal impurities (Al, Ga, and In), we consider three possible configurations, including the metal atom substituted for Zn (Al_{Zn}, Ga_{Zn}, and In_{Zn}), metal substituted for Sb (Al_{Sb}, Ga_{Sb}, and In_{Sb}), and interstitials (Al_i, Ga_i, and In_i). For F, only two configurations, F substituted for O (F_O), and F interstitial (F_i), were considered; F substituted for Zn, and Sb would cause very high formation energies due to large differences in their ionic radii.

Since Al, Ga, and In have one valence electron more than that of Zn, Al_{Zn}, Ga_{Zn}, and In_{Zn} are expected to behave as single donors. Fig. 6 shows these impurities are stable in the 1+ and neutral charge states with $\varepsilon(1+/0) \sim 4.28$–$4.39$ eV above the VBM. Among the three impurities, Ga_{Zn} exhibits the lowest formation energy, likely due to its ionic radius being closest to that of Zn and its similar electronic configuration ($3d^{10}4s^2$). While Al_{Zn}, Ga_{Zn}, and In_{Zn} act as single donors, they may be self-compensated by Al_{Sb}, Ga_{Sb}, and In_{Sb}, which may act as acceptors since Sb can be present in multiple oxidation states. Fig. 6 shows that Al_{Sb} is mostly stable in the neutral charge state, being electrically inactive for almost the entire range of the Fermi level, indicating that it is unlikely to act as a self-compensating center. Nevertheless, Ga_{Sb} and In_{Sb} can occur in the neutral, 1−, and 2− charge states, acting as deep acceptors. The transition levels associated with Ga_{Sb} are $\varepsilon(0/1-) = 3.22$ eV and $\varepsilon(1-/2-) = 3.92$ eV, and with In_{Sb} are $\varepsilon(0/1-) = 2.33$ eV and $\varepsilon(1-/2-) = 3.28$ eV. Although these acceptors are difficult to form for ε_F near the VBM due to their high formation energies, they can form in sizable concentrations under n-type conditions, indicating that they are likely to compensate for the donor impurities Ga_{Zn} and In_{Zn}. This means that donor doping with Ga and In is likely to be hindered from self-compensation. Self-compensation of metal doping was also observed in some ternary oxides such as $BaSnO_3$.[29] The interstitials Al_i, Ga_i, and In_i can donate up to three electrons to the neighboring O atoms and become triple donors. However, they have very high formation energies under O-rich and O-poor conditions. Thus, their concentrations are neglectable and unlikely to supply

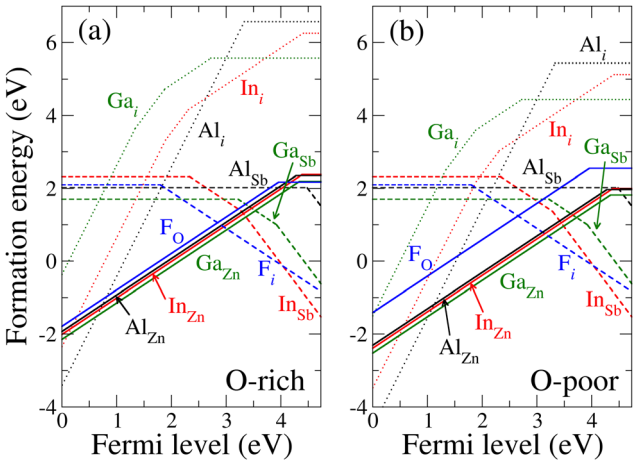

Fig. 6 Formation energy as a function of the Fermi level of Al, In, Ga, and F impurities in $ZnSb_2O_4$. The results are shown for (a) the O-rich limit and (b) the O-poor limit. The zero of the Fermi level corresponds to the VBM and CBM. Only segments corresponding to the lowest energy charge states are shown. The slope of each segment indicates the charge state. Kinks in the lines for the same defect indicate the thermodynamic transition levels.

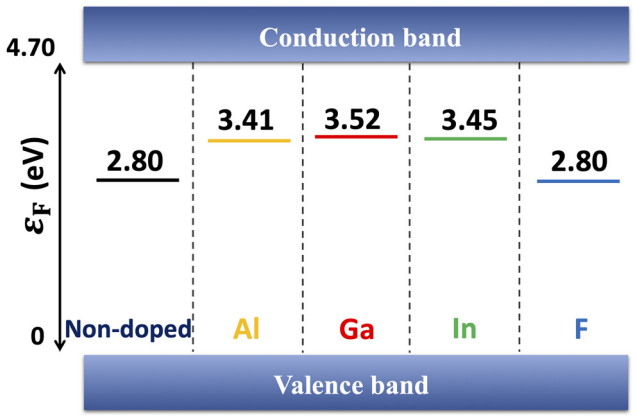

Fig. 7 Schematic illustration for the pinned Fermi level of intrinsic $ZnSb_2O_4$, and Al-, Ga-, In, and F-doped $ZnSb_2O_4$ obtained by charge neutrality conditions. The VBM is set to 0 eV.

electron carriers to the material. It is worth noting that the solubility of these metal impurities in $ZnSb_2O_4$ is limited by the formation of the corresponding metal oxides, *i.e.*, Al_2O_3, Ga_2O_3, and In_2O_3. As a result, the formation energy of the metal impurities under the O-poor conditions is lower than that under the O-rich conditions (Fig. 6), suggesting that metal doping is more feasible under the O-poor conditions.

Since F has one more valence electron than O, F_O is expected to act as a single donor. This is evident by its formation energy shown in Fig. 6, in which F_O occurs in 1+ and the neutral charge. The transition level $\varepsilon(1+/0) = 3.96$ eV, indicating that F_O is a deep donor. By contrast, when the F atom is located at the interstitial site (Fig. S7(b), ESI†), it can draw an electron from the nearby Sb atom to fill its electronic shell. Fig. 6 shows that F_i presents in the neutral and 1− charge states, acting as a deep acceptor with $\varepsilon(0/1-) = 1.80$ eV. These two F impurities (F_O^+ and F_i^-) are countercharged. They have comparable formation energies at the ε_F values near the middle of the band gap, indicating that self-compensation is likely to take place when doping with F. Due to the precipitating ZnF_2 phase, the formation energy of the F impurities is lower under the O-rich conditions than under the O-poor conditions. The O-rich conditions are, therefore, likely for F doping.

As discussed above, we found that the O-rich conditions were the most favorable n-type doping conditions for metal and F doping. By utilizing charge neutrality defined in eqn (3), we calculated the pinned Fermi level resulting from doping with the metals and F for the O-rich conditions using the formation energies of the respective impurity in various configurations as depicted in Fig. 6(b). The effect of dominant intrinsic defects, including V_{Zn}, V_{Sb}, and Zn_{Sb}, on charge neutrality, was also taken into account. Fig. 7 shows the pinned Fermi levels due to doping with Al, Ga, In, or F under the O-rich conditions at a temperature of 400 K. We find that Ga-doped $ZnSb_2O_4$ presents the highest pinned $\varepsilon_F = 3.52$ eV above the VBM among the metal dopants, while F-doped $ZnSb_2O_4$ yields pinned $\varepsilon_F = 2.80$ eV equal to that of the undoped $ZnSb_2O_4$. It was observed that the closer pinned ε_F to the middle of the band gap (~2.35 eV), the more insulating the material became. These findings indicate that Ga was the most favorable dopant for n-type doping. However, the pinned ε_F remained reasonably far from the conduction band edge, resulting in weak n-type conductivity with an electron carrier concentration of only $\sim 10^4$ cm^{-3}. Furthermore, Al and In doping produces very low electron carrier concentrations, suggesting they cannot serve as effective donors. Note that at higher growth temperatures, *e.g.*, 600–800 K, the pinned ε_F of the doped $ZnSb_2O_4$ is nearly unchanged. This indicates that it is very difficult to dope this ternary oxide into n-type.

The doping challenges encountered in $ZnSb_2O_4$ can be explained by several factors. Firstly, all the donor dopants are deep donors whose donor thermodynamic transition levels, or donor ionization energies, lie significantly (at least ~0.3 eV) below the CBM. This phenomenon impedes the fraction of dopants that can be ionized, thereby limiting the number of free carriers that can be contributed to the conduction band at a given temperature. Additionally, intrinsic properties of $ZnSb_2O_4$, such as its large bandgap and the absolute position of its conduction band edge, significantly influence the degree of ionization of donors. Secondly, the major donor impurities (Ga_{Zn}, Al_{Zn}, In_{Zn}, and F_O) will likely be compensated by intrinsic point defects acting as acceptors, such as Zn_{Sb}, V_{Zn}, and V_{Sb}. These point defects have low formation energies under n-type conditions. Finally, all donor impurities selected in this study suffered from self-compensation. Due to the comparable dopant concentration around the middle of the band gap between the donors and acceptors, Ga_{Zn}, Al_{Zn}, and In_{Zn} will likely be compensated by Ga_{Sb}, Al_{Sb}, and In_{Sb}, respectively. In contrast, F_O will be compensated by F_i. The resulting pinned ε_F coincidentally aligns with the ε_F observed in undoped $ZnSb_2O_4$. Another factor inhibiting a high concentration of

the dopant is solubility, which is the maximum concentration the impurity can realize at a given temperature. Despite the self-compensation of Ga, In, Al, and F impurities, their solubility in $ZnSb_2O_4$ is limited by the formation of Ga_2O_3, In_2O_3, Al_2O_3, and ZnF_2. Based on our results, we propose that with $ZnSb_2O_4$ it is very difficult to attain high electron carrier concentration by doping with Ga, In, Al, and F, which are already plausible when substituted for Zn. To efficiently dope this material into n-type, other impurity candidates such as hydrogen (H), tellurium (Te), or other approaches should be considered. In addition, investigating p-type dopability for this ternary oxide could prove to be a challenging task. It is also likely to suffer from doping asymmetry, which has been long studied and realized in many wide-band-gap semiconductors.[58,59] We assume this material is viable for n-type doping based on the Mullikan electronegativity approach and the low conduction band edge position. However, we need to explore other approaches for more accurate band edge positions, such as slab supercell models or interface calculations. Utilizing these methods would provide better suggestions for a more effective doping strategy in $ZnSb_2O_4$.

4. Conclusions

We have theoretically investigated the energetics and electronic properties of all intrinsic point defects and Al, Ga, In, and F impurities in $ZnSb_2O_4$ through the HSE06 hybrid density-functional calculations. Several fundamental bulk and electronic properties, such as the lattice parameters, formation enthalpy, band gap, band structure, band edge positions, and the density of states, have also been determined. We find that the HF fraction of 48% yields the calculated band gap and lattice parameters in good agreement with the experimental values. Our calculations for the energetics of the intrinsic point defects indicate that there are no shallow donor and shallow acceptor defects with low formation energies. The oxygen vacancy V_O has the lowest formation energy among the donor-type defects under the O-rich and O-poor conditions. However, it acts as a very deep acceptor, unlikely to provide free electron carriers to the conduction band. Moreover, electron carriers are likely to be compensated by the formation of V_{Zn} and Zn_{Sb}, which behave as dominant acceptors. Our analysis of the charge neutrality conditions estimates that the Fermi level of undoped $ZnSb_2O_4$ would be pinned in a range that is 2.39 eV to 2.80 eV above the VBM for the O-rich to O-poor growth conditions, respectively, suggesting that this material is semi-insulating.

We further investigate the possibility of enhancing free electron carriers by doping with Al, Ga, In, and F impurities, finding that Al_{Zn}, Ga_{Zn}, In_{Zn}, and F_O are single donors. Although Ga_{Zn} is the most viable donor impurity due to its lowest formation energy among other donor impurities, its concentration is reasonably low for the n-type conditions. Moreover, Ga_{Zn} would be compensated by Ga_{Sb}, which acts as an acceptor, thereby inhibiting high electron carrier concentration. The other donors Al_{Zn}, In_{Zn}, and F_O, also suffer from low solubility and self-compensation. The maximum pinned Fermi level of $\sim$3.52 above the VBM is attained in Ga-doped $ZnSb_2O_4$ under the O-poor conditions, resulting in a very low carrier concentration, which is insufficient for an effective n-type semiconductor. It is essential to consider other impurity candidates such as hydrogen (H), tellurium (Te), or other approaches for doping this material successfully. These issues should be further investigated. Our results presented here, nevertheless, are already paving the way for point defect engineering in this class of ternary oxides.

Conflicts of interest

There are no conflicts to declare.

Acknowledgements

This work was supported by the Graduate School of Kasetsart University. P. R. acknowledges the Thailand Research Fund (grant no. RSA6280068). S. J. was supported by (i) Suranaree University of Technology (SUT), (ii) Thailand Science Research and Innovation (TSRI), and (iii) National Science, Research and Innovation Fund (NSRF) (NRIIS Project Number 4366696). We thank RIKEN's supercomputing cluster system (HOKUSAI) and NSTDA Supercomputer Center (ThaiSC) for providing computing resources for this work.

References

1 P. Suttiyarak and A. Tubtimtae, *Appl. Surf. Sci.*, 2020, **527**, 146835.
2 M. Buddeesao, D. Raknual, A. Tubtimtae, V. Vailikhit and P. Teesetsopon, *Mater. Sci. Semicond. Process.*, 2020, **105**, 104713.
3 J. Sribenjawan, D. Raknual, V. Vailikhit, N. Kitisripanya and A. Tubtimtae, *Mater. Lett.*, 2019, **245**, 126–129.
4 C.-Q. Yi, J.-P. Zou, H.-Z. Yang and X. Leng, *Trans. Nonferrous Met. Soc. China*, 2018, **28**, 1980–2001.
5 B. Mendoza-Sánchez, T. Brousse, C. Ramirez-Castro, V. Nicolosi and P. S. Grant, *Electrochim. Acta*, 2013, **91**, 253–260.
6 T. P. Gujar, V. R. Shinde, C. D. Lokhande and S.-H. Han, *J. Power Sources*, 2006, **161**, 1479–1485.
7 P. A. Shinde, A. C. Lokhande, N. R. Chodankar, A. M. Patil, J. H. Kim and C. D. Lokhande, *Electrochim. Acta*, 2017, **224**, 397–404.
8 S. E. Moosavifard, M. F. El-Kady, M. S. Rahmanifar, R. B. Kaner and M. F. Mousavi, *ACS Appl. Mater. Interfaces*, 2015, **7**, 4851–4860.
9 D. C. Look, G. C. Farlow, P. Reunchan, S. Limpijumnong, S. B. Zhang and K. Nordlund, *Phys. Rev. Lett.*, 2005, **95**, 225502.
10 S.-Y. Kuo, W.-C. Chen, F.-I. Lai, C.-P. Cheng, H.-C. Kuo, S.-C. Wang and W.-F. Hsieh, *J. Cryst. Growth*, 2006, **287**, 78–84.
11 M. Tortosa, F. J. Manjón, M. Mollar and B. Marí, *J. Phys. Chem. Solids*, 2012, **73**, 1111–1115.

12 S. Mathur, M. Veith, M. Haas, H. Shen, N. Lecerf, V. Huch, S. Hüfner, R. Haberkorn, H. P. Beck and M. Jilavi, *J. Am. Ceram. Soc.*, 2001, **84**, 1921–1928.
13 S. D. Shenoy, P. A. Joy and M. R. Anantharaman, *J. Magn. Magn. Mater.*, 2004, **269**, 217–226.
14 T. Omata, N. Ueda, K. Ueda and H. Kawazoe, *Appl. Phys. Lett.*, 1994, **64**, 1077–1078.
15 Z. Mousavi, F. Soofivand, M. Esmaeili-Zare, M. Salavati-Niasari and S. Bagheri, *Sci. Rep.*, 2016, **6**, 20071.
16 A. K. Jibin, M. V. Reddy, G. V. Subba Rao, U. V. Varadaraju and B. V. R. Chowdari, *Electrochim. Acta*, 2012, **71**, 227–232.
17 J. R. Gavarri, R. Chater and J. Ziółkowski, *J. Solid State Chem.*, 1988, **73**, 305–316.
18 A. Mekap, P. R. Das and R. N. P. Choudhary, *Adv. Mater. Lett.*, 2014, **5**, 152–156.
19 S. Khalid, F. Saleemi, R. Zia, S. Anjum, F. Bashir, N. Tahir and A.-U. Haq, *Optik*, 2016, **127**, 10172–10179.
20 M. Zhong, Z. Wei, X. Meng, F. Wu and J. Li, *RSC Adv.*, 2015, **5**, 2429–2433.
21 D. Raknual, S. Charoenphon, P. Reunchan and A. Tubtimtae, *Electrochim. Acta*, 2021, **389**, 138773.
22 V. E. Alexandrov, E. A. Kotomin, J. Maier and R. A. Evarestov, *Eur. Phys. J. B*, 2009, **72**, 53–57.
23 A. Janotti, J. B. Varley, M. Choi and C. G. Van de Walle, *Phys. Rev. B: Condens. Matter Mater. Phys.*, 2014, **90**, 085202.
24 U. S. Shenoy and D. K. Bhat, *J. Phys. Chem. Solids*, 2021, **148**, 109708.
25 F. Maldonado and A. Stashans, *J. Phys. Chem. Solids*, 2017, **102**, 136–141.
26 J. A. Dawson, J. H. Harding, H. Chen and D. C. Sinclair, *J. Appl. Phys.*, 2012, **111**, 094108.
27 P. Erhart and K. Albe, *J. Appl. Phys.*, 2008, **104**, 044315.
28 L. Weston, L. Bjaalie, K. Krishnaswamy and C. G. Van de Walle, *Phys. Rev. B*, 2018, **97**, 054112.
29 D. O. Scanlon, *Phys. Rev. B: Condens. Matter Mater. Phys.*, 2013, **87**, 161201.
30 K. Krishnaswamy, B. Himmetoglu, Y. Kang, A. Janotti and C. G. Van de Walle, *Phys. Rev. B*, 2017, **95**, 205202.
31 T. R. Paudel, A. Zakutayev, S. Lany, M. d'Avezac and A. Zunger, *Adv. Funct. Mater.*, 2011, **21**, 4493–4501.
32 M. N. Amini, H. Dixit, R. Saniz, D. Lamoen and B. Partoens, *Phys. Chem. Chem. Phys.*, 2014, **16**, 2588–2596.
33 K. Simalaotao, P. Reunchan, N. Umezawa, J. T-Thienprasert and A. Boonchun, *J. Appl. Phys.*, 2019, **125**, 165703.
34 J. Heyd, G. E. Scuseria and M. Ernzerhof, *J. Chem. Phys.*, 2003, **118**, 8207–8215.
35 G. Kresse and J. Furthmüller, *Comput. Mater. Sci.*, 1996, **6**, 15–50.
36 C. Freysoldt, J. Neugebauer and C. G. Van de Walle, *Phys. Rev. Lett.*, 2009, **102**, 016402.
37 M. Gajdoš, K. Hummer, G. Kresse, J. Furthmüller and F. Bechstedt, *Phys. Rev. B: Condens. Matter Mater. Phys.*, 2006, **73**, 045112.
38 A. J. Jackson and A. Walsh, *J. Mater. Chem. A*, 2014, **2**, 7829–7836.
39 M. Binnewies and E. Milke, *Thermochemical data of elements and compounds*, Wiley Online Library, 2002.
40 M. V. Putz, N. Russo and E. Sicilia, *Theor. Chem. Acc.*, 2005, **114**, 38–45.
41 L. A. Burton and A. Walsh, *J. Solid State Chem.*, 2012, **196**, 157–160.
42 K. Momma and F. Izumi, *J. Appl. Crystallogr.*, 2011, **44**, 1272–1276.
43 B. Dickens, *J. lnorg. Nucl. Chem.*, 1965, **27**, 1509–1515.
44 G. Henkelman, A. Arnaldsson and H. Jónsson, *Comput. Mater. Sci.*, 2006, **36**, 354–360.
45 R. F. Bader, *Acc. Chem. Res.*, 1985, **18**, 9–15.
46 V. Srikant and D. R. Clarke, *J. Appl. Phys.*, 1998, **83**, 5447–5451.
47 H. Ohta and H. Hosono, *Mater. Today*, 2004, **7**, 42–51.
48 M. A. Butler and D. S. Ginley, *J. Electrochem. Soc.*, 1978, **125**, 228.
49 Y. Xu and M. A. A. Schoonen, *Am. Mineral.*, 2000, **85**, 543–556.
50 P. Reunchan, A. Boonchun and N. Umezawa, *Phys. Chem. Chem. Phys.*, 2016, **18**, 23407–23411.
51 C. G. V. d Walle and J. Neugebauer, *J. Appl. Phys.*, 2004, **95**, 3851–3879.
52 S. Charoenphon, A. Boonchun, D. Jarukanont, J. T-Thienprasert and P. Reunchan, *RSC Adv.*, 2020, **10**, 19648–19654.
53 A. Janotti and C. G. Van de Walle, *J. Cryst. Growth*, 2006, **287**, 58–65.
54 R. Shannon, *Acta Crystallogr., Sect. A: Cryst. Phys., Diffr., Theor. Gen. Crystallogr.*, 1976, **32**, 751–767.
55 F. Oba, M. Choi, A. Togo and I. Tanaka, *Sci. Technol. Adv. Mater.*, 2011, **12**, 034302.
56 J.-H. Yang, J.-S. Park, J. Kang, W. Metzger, T. Barnes and S.-H. Wei, *Phys. Rev. B: Condens. Matter Mater. Phys.*, 2014, **90**, 245202.
57 D. A. Neamen, *Semiconductor physics and devices: basic principles*, McGraw-Hill, 2003.
58 V. Avrutin, D. J. Silversmith and H. Morkoç, *Proc. IEEE*, 2010, **98**, 1269–1280.
59 Y. Yan and S.-H. Wei, *Phys. Status Solidi B*, 2008, **245**, 641–652.